Harmonic phase-sensitive detection for quartz-enhanced photoacoustic-thermoelastic spectroscopy

Mengpeng Hu [a,b], Dongqing Zhang [a,b], Hui Zhang [a,b], Yu Liu [a,c], Weibiao Wang [a,b], Qiang Wang [a,b,c,*]

[a] State Key Laboratory of Applied Optics, Changchun Institute of Optics, Fine Mechanics and Physics, Chinese Academy of Sciences, Changchun 130033, China
[b] University of Chinese Academy of Sciences, Beijing 100049, China
[c] Key Laboratory of Advanced Manufacturing for Optical Systems, Changchun Institute of Optics, Fine Mechanics and Physics, Chinese Academy of Sciences, Changchun 130033, China

ARTICLE INFO

ABSTRACT

Quartz tuning fork (QTF)-based techniques of photoacoustic spectroscopy and thermoelastic spectroscopy play a significant role in trace gas sensing due to unique high sensitivity and compactness. However, the stability of both techniques remains plagued by the inevitable and unpredictable laser power variation and demodulation phase variation. Herein, we investigate the phase change of a QTF when integrating both techniques for enhanced gas sensing. By demonstrating harmonic phase-sensitive methane detection as an example, we achieve stable gas measurement at varying laser power (2.4–9.4 mW) and varying demodulation phase (-90–$90°$). Besides, this method shows more tolerance to resonant frequency drift, contributing to a small signal fluctuation of ≤ 6.4 % over a wide modulation range (>10 times of the QTF bandwidth). The realization of harmonic-phase detection allows strengthening the stability of QTF-based sensors in a simple manner, especially when stable parameters, such as laser power, demodulation phase, even resonant frequency, cannot always be maintained.

1. Introduction

Trace gas sensing with high sensitivity and high robustness is imperative in numerous applications such as industrial production safety [1,2], environmental monitoring [3–5] and respiratory analysis [6,7] Among a large panorama of available technologies, optical detection highlights itself with promising sensitivity, robustness, and versatility. Quartz-enhanced photoacoustic spectroscopy (QEPAS), as a representative indirect absorption spectroscopy technique, was firstly proposed in 2002 [8]. The acoustic wave generated by a modulated laser beam absorbed by the analyte is converted into electrical signal by a quartz tuning fork (QTF) based on its piezoelectric properties. Light-induced thermoelastic spectroscopy (LITES) was firstly proposed by Ma et al. in 2018 [9]. Unlike QEPAS, the modulated laser carrying gas absorption information directly focuses on the QTF surface, producing modulated localized heating, which generates thermoelastic expansion of the quartz crystal and, in turn, piezoelectric charge distribution on the quartz prongs. The use of QTFs as transducers not only has important advantages of exquisite simplicity, compact size, and low cost, but also

enables signal conversion from acoustic waves or thermoelastic expansions at its resonant mode, which contributes to a high sensitivity by intrinsically isolating most accompanying noise outside its narrow bandwidth. QTF-based sensors have proven promising prospect as highly competitive candidates for the sensitive detection of various inorganic and organic trace gases [10–18].

Recent years have witnessed remarkable progress in QTF-based spectroscopy, such as the analysis of resonance modes [19,20], the optimization of optical path structure [21–24], all-fiber QEPAS [25–27], customized QTFs [28,29], etc. Subsequently, many new QTF-based technologies have emerged to achieve high performance in gas sensing. For instance, Wang et al. developed a gas sensor based on doubly resonant PAS, in which the acoustic and optical waves are simultaneously enhanced using combined optical and acoustic resonators in a centimeter-long configuration, and finally achieved a state-of-the-art NEA of 5.7×10^{-13} cm^{-1} [11] and a minimum detection limit down to 10 ppb for caustic sulfuretted hydrogen [30]. Wei et al. reported the development of a dielectric/metallic film-coated QTF with high responsivity and extended working spectral range across

---

* Corresponding author at: State Key Laboratory of Applied Optics, Changchun Institute of Optics, Fine Mechanics and Physics, Chinese Academy of Sciences, Changchun 130033, China.
E-mail address: wangqiang@ciomp.ac.cn (Q. Wang).

1.65–10.34 μm, demonstrating intriguing possibility in spectroscopic systems [31]. Qiao et al. developed a trace gas detection technique of quartz-enhanced photoacoustic-thermoelastic spectroscopy, which makes full use of the laser power passing through the QEPAS system to irradiate the root of the same QTF for enhanced performance by simultaneously exciting its thermoelastic effect [32].

For both QEPAS and LITES, the signal amplitude is positively associated with laser power. Although this specific characteristic provides a simple way to improve the sensing sensitivity by directly employing state-of-the-art high-power laser sources [33–35], the laser fluctuation or intensity noise could also be introduced into signal in practical implementation. Stabilizing the optical power remains challenging, especially for remote sensing after long-distance transmission with inevitable and irregular scattering, transmission loss, and even unstable instrument operation. This is a decisive obstacle limiting the promotion and development of QTF-based sensors for applications in harsh environments. Usually the fluctuations caused by laser intensity can be simply compensated by using a photodetector or an optical power meter [36], however, at the expense of extra detection errors, high-cost, and complexity. In addition, with the simultaneous measurement of the first ($1f$) and the second ($2f$) harmonic signals of a single or two QTFs, $2f/1f$ method can eliminate the instability of light intensity [37,38]. Nonetheless, the frequency mismatch between the two QTFs or/and the obvious responsivity attenuation of a QTF when its narrow bandwidth embraces two separate frequencies have to be fully considered. In addition, the variation of demodulation phase is another factor that affects the measurement precision of QEPAS and LITES technologies. Although the phase of the frequency reference generated by the circuit is relatively stable in laboratory, the phase of the photoacoustic or light-induced thermoelastic signal could be fluctuated by other factors in practical applications, such as temperature variation [39] and the presence of gas interference [40]. Hence, the demodulation phase needs to be re-optimized to maintain its stability. The method of using orthogonal references to obtain the modulus of signal is adopted to avoid such influences [41], however, at the cost of expensive and complex circuits, and reduced signal amplitude.

In this work, we report another alternative route to a high immunity to laser power fluctuation and demodulation phase variation by demonstrating harmonic phase-sensitive detection of QTF signal, which comprises photoacoustic and thermoelastic components of a single QTF for enhanced response. In addition to inheriting the aforementioned advantages of traditional QTF-based methods, this strategy also has a high immunity to demodulation phase instability. As an example, we demonstrate stable phase demodulation from a fluctuant $1f$ signal for trace CH_4 sensing, even at a large laser power variation of 6 dB (2.4–9.4 mW) and a varying demodulation phase from $-90°$ to $90°$. We also experimentally investigated the influence of QTF resonant frequency drift on the phase signal, showing a more stable performance compared to the widely used QTF-based sensors with intensity demodulation.

2. Working principle

Fig. 1 illustrates the fundamental concept of the first harmonic phase angle ($1f$-PA, abbreviated as θ_{1f}) of quartz-enhanced photoacoustic-thermoelastic spectroscopy. Initially, a modulated laser beam traverses the gap between the two prongs of a QTF to stimulate photoacoustic signal. The beam is then reflected by a concave reflector and focuses on the root of the same QTF (point A in Fig. 3 (d)) for maximum light-induced thermoelastic signal generation [42,43]. The synergy of both regimes forms the QTF output, which is then mixed with the in-phase and quadrature references, respectively, at the laser modulation frequency to retrieve the first harmonic phase, i.e., the θ_{1f} signal, after arctangent process.

For most QTF-based gas sensing, wavelength modulation spectroscopy with harmonic detection has been well established and widely used due to its high signal-to-noise ratio. Modulation applied on the commonly used diode lasers usually involves a low-frequency linear scanning current and a rapid sinusoidal dither, which simultaneously modulates the laser intensity I_0 and frequency ν [44]:

$$\begin{cases} I_0 = \bar{I}_0[1 + i_1\cos(2\pi f_m t + \varphi_1)] \\ \nu = \nu_0 + \nu_1\cos(2\pi f_m t) \end{cases} \tag{1}$$

where f_m is the modulation frequency, I_0 and i_1 are the average intensity and relative intensity modulation amplitude (normalized by I_0), ν_0 and ν_1 are the central laser frequency and its modulation amplitude, φ_1 is the phase shift between intensity modulation and frequency modulation.

With the Beer-Lambert law considered, the photoacoustic signal can be expressed as [45]:

$$S_{PA} = G_{PA}I_0 l_1 \alpha(\nu) \tag{2}$$

where G_{PA} is the conversion coefficient of the photoacoustic signal to QTF piezoelectric voltage, l_1 is the effective absorption length of photoacoustic signal, including the path length inside the acoustic resonator and the gap between the two prongs of the QTF. $\alpha(\nu)$ is the absorption coefficient, which can be expanded into Fourier cosine series [46]:

$$\alpha(\nu) = \alpha(\nu_0 + \nu_1\cos(2\pi f_m t)) = \sum_{k=0}^{\infty} H_k(\nu_0, \nu_1)\cos(2\pi f_m t) \tag{3}$$

where H_k is the kth Fourier coefficient [44].

After photoacoustic excitation, the laser focuses back on the same QTF. Thus, the thermoelastic signal has a phase delay φ_2 because of the extra laser transmission path. Therefore, the laser intensity I_0' and frequency ν' for thermoelastic signal excitation can be expressed as:

$$\begin{cases} I_0' = \bar{I}_0[1 + i_1\cos(2\pi f_m t + \varphi_1 + \varphi_2)] \\ \nu' = \nu_0 + \nu_1\cos[2\pi f_m t + \varphi_2] \end{cases} \tag{4}$$

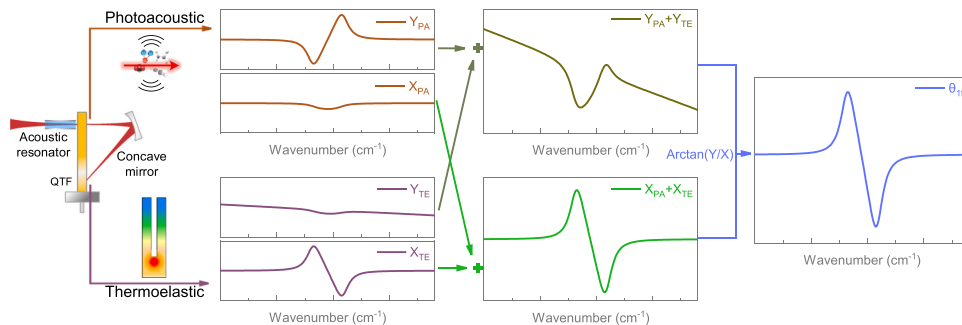In the case of thin absorption, the thermoelastic signal can be expressed as [31]:

Fig. 1. Principle of harmonic phase-sensitive quartz-enhanced photoacoustic-thermoelastic spectroscopy.

$$S_{TE} = G_{TE}I'_0[1 - l_2\alpha(\nu')] \tag{5}$$

where G_{TE} is the conversion coefficient of the thermoelastic signal to the QTF piezoelectric voltage, l_2 is the effective absorption length of thermoelastic signal, including the length of laser beam passing through the gas chamber and the inner length when the laser beam reenters into the gas chamber after reflection. $\alpha(\nu')$ is the absorption coefficient of the target gas, which can be expanded into Fourier cosine series:

$$\alpha(\nu') = \alpha(\nu_0 + \nu_1\cos(2\pi f_m t + \varphi_2)) = \sum_{k=0}^{\infty} H_k(\nu_0, \nu_1)\cos(2\pi kf_m t + k\varphi_2) \tag{6}$$

where H_k is the same as that in Eq. (3).

The superposition of the photoacoustic and thermoelastic signals constructs the final QTF output as

$$S = S_{PA} + S_{TE} \tag{7}$$

The X and Y components of its first harmonic signal, namely X_{1f} and Y_{1f}, can be obtained by demodulating S using a pair of orthogonal homo-frequency references.

$$\begin{cases} X_{1f} = \dfrac{G_{PA}\bar{I}_0}{2}X_{1f}^{PA} + \dfrac{G_{TE}\bar{I}_0}{2}X_{1f}^{TE} \\ Y_{1f} = \dfrac{G_{PA}\bar{I}_0}{2}Y_{1f}^{PA} + \dfrac{G_{TE}\bar{I}_0}{2}Y_{1f}^{TE} \end{cases} \tag{8}$$

the details of $Y^{PA}{}_{1f}$ $Y^{TE}{}_{1f}$, $X^{PA}{}_{1f}$ $X^{TE}{}_{1f}$ are described in Appendix A. And the corresponding first harmonic phase, θ_{1f}, can be retrieved by using arctangent operation:

$$\theta_{1f} = \tan^{-1}\left(\frac{Y_{1f}}{X_{1f}}\right) \tag{9}$$

By combing the first set of equations in Appendix A, Eqs. (8); (9), we rearrange the formula in arctangent form to separate the phase between frequency reference and laser frequency modulation, φ_3. The expression of θ_{1f} can be shown as

$$\theta_{1f} = \tan^{-1}\left\{ \frac{\tan(\varphi_3) - \tan(\theta'_{1f})}{1 + \tan(\varphi_3) * \tan(\theta'_{1f})} \right\} = \varphi_3 - \theta'_{1f} \tag{10}$$

where θ'_{1f} can be expressed as:

$$\theta'_{1f} = \tan^{-1}\left(\frac{G_{PA}Y_{1f}^{PA0} + G_{TE}Y_{1f}^{TE0}}{G_{PA}X_{1f}^{PA0} + G_{TE}X_{1f}^{TE0}} \right) \tag{11}$$

where Y_{1f}^{PA0}, Y_{1f}^{TE0}, X_{1f}^{PA0}, X_{1f}^{TE0} are the expressions of $Y^{PA}{}_{1f}$, $Y^{TE}{}_{1f}$, $X^{PA}{}_{1f}$, $X^{TE}{}_{1f}$, respectively, when φ_3 equals to zero. The details of $Y^{PA0}{}_{1f}$, $Y^{TE0}{}_{1f}$, $X^{PA0}{}_{1f}$, $X^{TE0}{}_{1f}$ are described in Appendix A.

In Eq. (11), all the parameters are constant once the system is assembled, except for the absorption-related Fourier absorption coefficients, i.e., H_k. That is, phase change can only be generated by gas absorption. Scanning the central laser frequency across the absorption feature enables us to know the harmonic-phase spectroscopic response to laser-gas molecule interaction. In the implementation, selection of peak-to-peak value of θ_{1f} to determine the signal amplitude inherently eliminates φ_3, allowing the phase measurement independent from the demodulation phase as well as the laser power. Usually, the values of G_{PA} and G_{TE}, for the same QTF, are both affected by frequency f_m by a similar proportion. Hence, the influences of G_{PA} and G_{TE} variation, in the case of resonant frequency drift, might counteract each other to a certain extent. This characteristic could in turn improve the immunity of θ_{1f} sensors to environment changes, such as operation temperature [13] and pressure [28] that could change the QTF resonant frequency.

3. Experimental setup

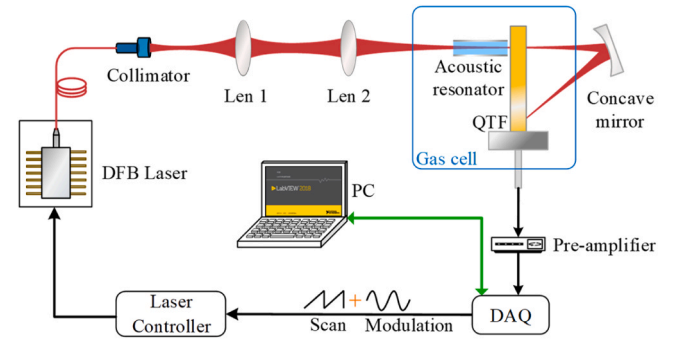Fig. 2 depicts the schematic of the quartz-enhanced photoacoustic-

Fig. 2. Schematic of the experimental setup. DFB laser, distributed feedback laser; QTF, quartz tuning fork; DAQ, data acquisition card.

thermoelastic setup for phase-sensitive detection of trace gas. A distributed feedback laser (DFB) laser with a center wavelength around 1653.73 nm, targeting methane measurement as an example, is employed as the laser source, which is driven by a commercial laser diode controller (LDC502, Standford Research Systems). The laser scanning and modulation parameters are determined by a software-based function generator using a multifunctional data acquisition card (DAQ) (USB-6356, NI). A fiber collimator couples the wavelength modulated laser from fiber into free space. Two convex lenses further shape the beam so that the laser can pass through a resonance tube (length, 4.7 mm; inner diameter, 0.6 mm), for enhancing the acoustic wave, and a QTF successively without touching any surfaces. After the QTF, the laser beam focuses back on the QTF by a concave reflector, which can maximize the thermoelastic signal by adjusting the laser spot on the root between the two fork prongs [42,43]. The blue box in the Fig. 2 indicates the boundary of gas cell. The piezoelectric signal induced by the synergy of photoacoustic and thermoelastic effect is amplified with a home-made trans-impedance preamplifier before digitization. The QTF signal acquisition as well as the laser controller is governed by the same DAQ driven by a home-developed LabVIEW program, which also integrates several subVIs for subsequent data averaging and phase demodulation. To a certain extent, the QTF works like a photodetector when performing LITES. Hence, similarly, the residual amplitude modulation of a diode laser could generate a background that pedestal on the signal [39,44,47]. Differently, the immunity to laser power or/and demodulation phase fluctuation can be maintained thanks to the θ_{1f} process (see Appendix B) for the baselines.

4. Experimental results

4.1. Parameter optimization of θ_{1f} signal

Due to the narrow bandwidth of a QTF, it is necessary to characterize its resonant frequency for the best performance before performing gas sensing. By filling the gas cell with CH_4/N_2 of a fixed concentration, we measured the responses of the first harmonic intensity (1f) and the first harmonic phase angle (θ_{1f}) to the modulation frequency as illustrated in Fig. 3(a). Its resonant frequency of f_0=32.7649 kHz and bandwidth of Δf=5.6 Hz are determined by analyzing the frequency-response curve of 1f conforming to a Lorentzian shape. It is worth noting that the θ_{1f} response curve shows a relatively flat profile because of the phase retrieval process (Eq. (11)) in which the QEPAS and LITES response curves could be counteracted to a certain extent. The uneven part is probably caused by a mismatch between photoacoustic and thermoelastic responses. We further experimentally verified this hypothesis by separately measuring the frequency responses of photoacoustic and thermoelastic 1f signals with the normalized results shown in Fig. 3(b). The residual between the photoacoustic and thermoelastic 1f curves is nearly consistent with the frequency response shape of the θ_{1f} signal. Lorentzian fitting to the curves in Fig. 3(b) shows that the photoacoustic
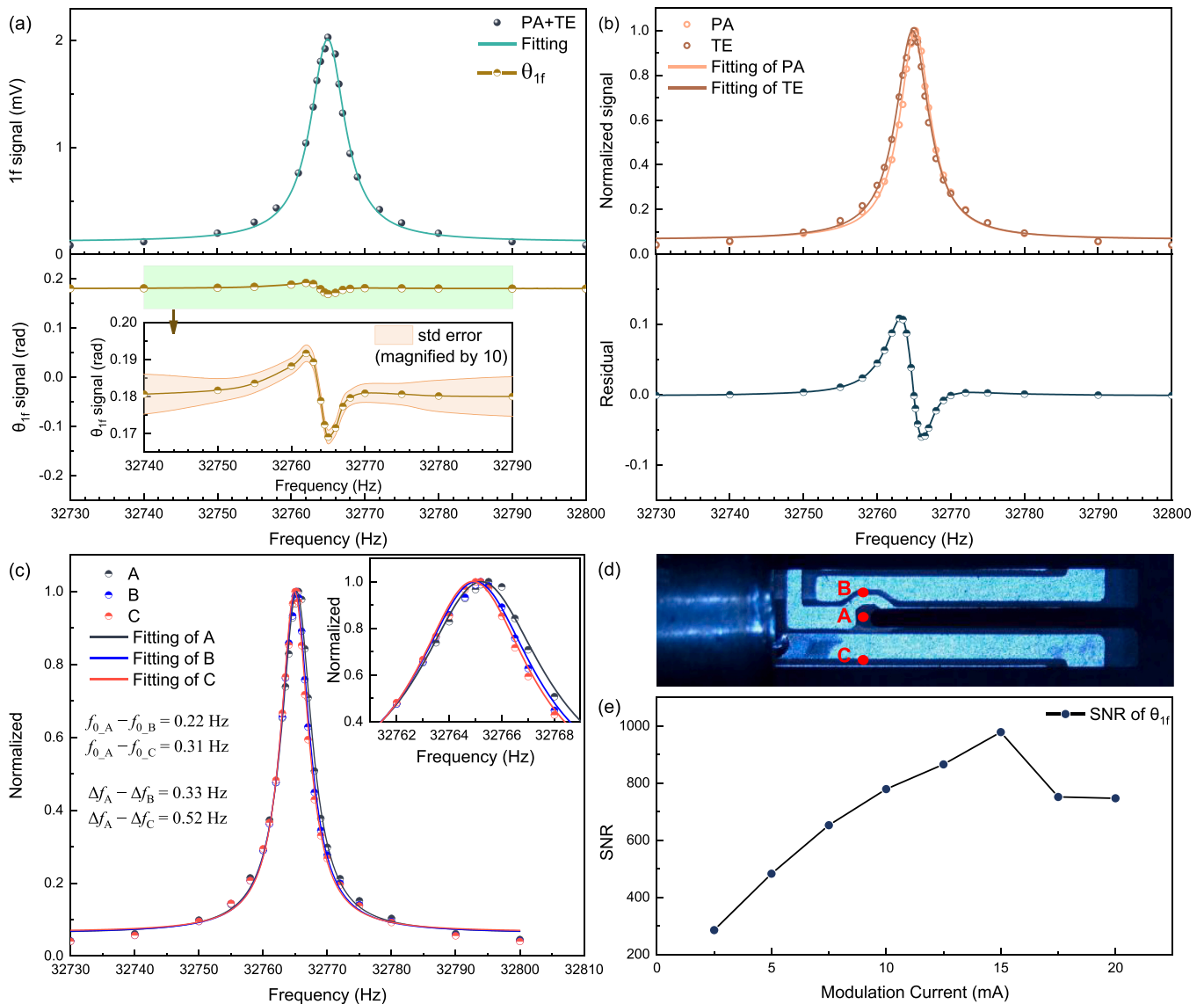
Fig. 3. (a) Frequency response curves of the photoacoustic-thermoelastic 1f signal and θ_{1f} signal. Inset: zoomed-in view in the vicinity of response frequency. The yellow shaded area represents the standard-error interval for 30 measurements, which is scaled up by tenfold for clarity. (b) Frequency responses of normalized photoacoustic and thermoelastic 1f signals. (c) Frequency responses of normalized thermoelastic 1f signal when the laser hits points A, B and C, respectively. Inset: zoomed-in view in the vicinity of response frequency. (d) Locations of points A, B and C. (e) The SNR of θ_{1f} versus the modulation current applied on the laser. All the experimental data above was extracted from their corresponding spectra after removing the baselines measured for pure N_2.

1f response has a resonant frequency of $f_{0\text{-PA}}$=32.7652 kHz and a bandwidth of Δf_{PA}=5.06 Hz, while the 1f thermoelastic response has a resonant frequency of $f_{0\text{-TE}}$=32.7648 kHz and a bandwidth of Δf_{TE}=5.45 Hz. Usually, the QTF resonator model equates the two tuning fork prongs to two freely vibrating masses coupled at the root. This model demonstrated that different forces on the two prongs of QTF cause changes in the amplitude ratio of the two prongs and finally affect the resonant frequency of QTF [48,49]. Therefore, the slight differences (0.4 Hz in resonant frequency and 0.39 Hz in bandwidth) in our case are likely due to the photoacoustic excitation close to the tip and/or the thermoelastic excitation at the root are not strictly located in the middle of two prongs, resulting in inconsistent response of the two prongs. In order to preliminarily verify this, we manually shifted the hit point from the maximum thermoelastic excitation one (point A, shown in Fig. 3(d)) to points B and C. The observation of frequency responses (Fig. 3(c)) shows that the excitation separation causes a resonant frequency shift of ~0.3 Hz and a bandwidth change of ~0.5 Hz even only thermoelastic excitation exists. This feature offers the possibility of adjusting the

bandwidth and resonant frequency of the thermoelastic signal by the laser spot position.

In Fig. 3(a), within the modulation range of 70 Hz (32,730–32,800 Hz), i.e., over 10 times of the Δf for 1f, the maximum influence of frequency shift on θ_{1f} is $\leq$ 6.4 %. On the contrary, the 1f signal is dramatically reduced by 96 % under the same conditions. That is to say, the proposed θ_{1f} method holds more tolerance to resonant frequency shift, which has been a long-standing issue for practical application of traditional QTF-based sensors. Further decreased influence can be expected if inconsistency between the photoacoustic and thermoelastic frequency responses could be suppressed by finely adjusting the position of the acoustic wave and light-induced thermoelastic expansion to balance the driving force on the two QTF prongs. However, as the harmonic phase is derived from 1f signal, according to Eq. (9), θ_{1f} will decline in SNR when the resonant frequency shifts if non-common-mode noise (e.g., the thermal noise of circuit and QTF, and the shot noise of QTF) dominates for the X and Y components of 1f. After experimental assessment, the best SNR of θ_{1f} signal locates at the 1f peak

(shown in inset of Fig. 3(a)). Thus, the resonant frequency in $1f$ demodulation manner, i.e., 32.7649 kHz was still chosen as the modulation frequency for the following experiments. Moreover, harmonic signal SNR of QTF-based sensors also depends on the modulation depth of the laser source, which can be adjusted by varying the modulation current applied on the laser [50]. As shown in Fig. 3(e). the optimal modulation current was found to be 15 mA by measuring the θ_{1f} SNR at different modulation currents for the selected modulation frequency and a fixed CH_4 concentration of 5000 ppm.

4.2. Immunity to the fluctuation of laser power and demodulation phase

The theoretical analysis in *Section 2* predicts the immunity of θ_{1f} signal to both laser power and demodulation phase fluctuations. We verify these characteristics by separately changing the excitation laser power and the LIA demodulation phase. A tunable attenuator and a coupler (50:50) were inserted in series between the DFB laser and the fiber collimator. One port of the coupler was connected to the collimator for the $1f$ or θ_{1f} signal excitation with 5000 ppm CH_4 sealed in the gas cell, and the other port was used for power monitoring with the results shown in Fig. 4. The blue line in the upper panel of Fig. 4(a) indicates the monitored four different laser power levels, which were adjusted by the tunable attenuator and lasted more than 1600 s in total. Zooming into part of the power monitoring result shows that only the laser scanning part was measured without the fast modulation part, which can be considered as the averaged laser power during the scanning cycle. This is

mainly because of the limited response bandwidth (~15 Hz) of our optical power meter (3A-QUAD, Ophir Optronics). The bottom panel of Fig. 4(a) shows the synchronously demodulated $1f$ signal (green line) and θ_{1f} signal (red line). The $1f$ signal decreases proportionally with the power reduction, while the θ_{1f} signal remains constant. Fig. 4(b) and (c) depict the measured representative baseline-subtracted $1f$ spectra and θ_{1f} spectra, respectively, under different averaged powers of 2.4, 4.1, 6.9, and 9.4 mW. It is worth noting that the baselines of $1f$ spectra for subtraction have to be measured separately for each laser power, whiel a single measurement is sufficient for θ_{1f} spectra process thanks to its excellent stability, which has also been confirmed by the relatively stable θ_{1f} amplitude at varying laser power (see Appendix B). However, after accessing the θ_{1f} signal SNR under different laser powers as shown in Fig. 4(d), it is of interest to observe that the θ_{1f} signal SNR increases proportionally to laser power, which can be roughly described by an obvious linear relationship with an R-square of 0.98. It is likely that the random noise, such as the thermal noise of the QTF, the white noise of the preamplifier, and the phase noise of the laser, dominates during the phase retrieval operation when the laser power decreases, corresponding to a reduced SNR for the $1f$ signal. Hence, similar to the traditional $1f$ detection, the SNR of θ_{1f} detection can be improved by simply boosting the laser power. Differently, the SNR improvement using this strategy replies on suppressing the noise level rather than increasing the signal amplitude.

The influence of varying demodulation phase on $1f$ signal and θ_{1f} signal was investigated for comparison. CH_4/N_2 mixture with a
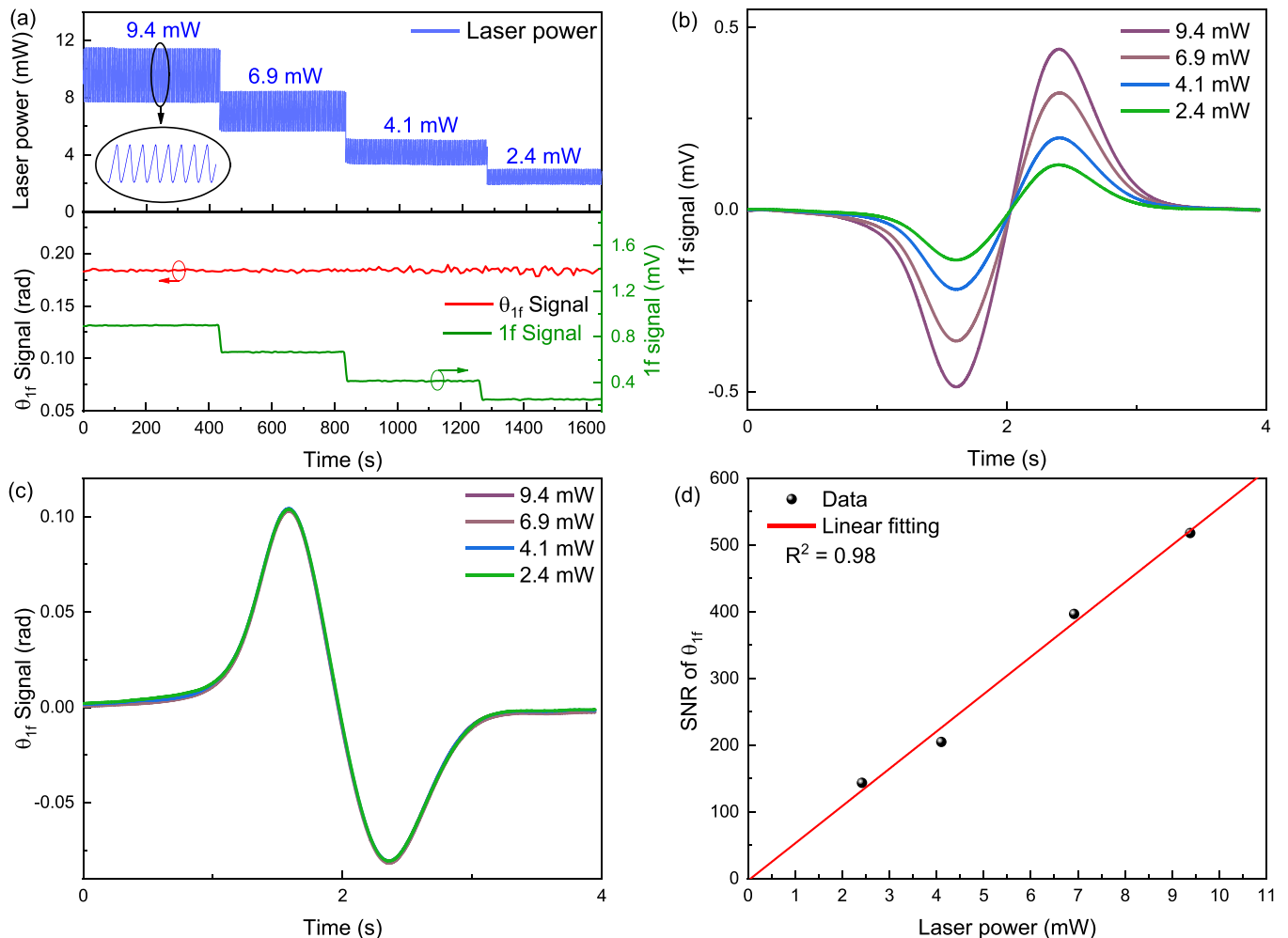

Fig. 4. (a) Influences of power variations on $1f$ signal and θ_{1f} signal. Inset: Zoom-in part of the monitored laser power with an averaged value of 9.4 mW. (b) Baseline-subtracted $1f$ spectra and (c) θ_{1f} spectra under different laser powers. (d) θ_{1f} SNR as a function of laser power.

concentration of 2000 ppm was used as an example. Fig. 5(a) depicts the recorded results with the demodulation phase adjusted from –90° to 90°. As shown in the upper panel of Fig. 5(a), the 1f signal monotonically increases from 0.07 mV to 0.51 mV when the demodulation phase changes from –90° to 0°, while the 1f signal monotonically decreases back to the original value with demodulation phase from 0° to –90°. On the contrary, the θ_{1f} signal, as shown in the bottom panel of Fig. 5(a), remains quite stable throughout the demodulation phase adjustment. Fig. 5(b) and (c) illustrate the measured representative original 1f spectra and θ_{1f} spectra, respectively, under several typical demodulation phases. The demodulation phase variation only causes the vertical shifts of θ_{1f} signal without affecting its peak-to-peak value, therefore proving the high immunity of the θ_{1f} method to demodulation phase fluctuation. Meanwhile we calculated the error bars of θ_{1f} under different demodulation phases as shown in Fig. 5(d), indicating that the SNR of θ_{1f} is not affected by demodulation phase.

4.3. Performance assessment of θ_{1f} methane measurement

We further conducted a quantitative analysis of how this technique responds to varying methane gas concentration. Different concentrations of methane were prepared using a commercial gas mixer (Sonimix 7100, LNI Swissgas) with concertation-certified CH_4/N_2 sample. Fig. 6 (a) shows the representative θ_{1f} spectra under four concentrations of CH_4, i.e., 100 ppm, 800 ppm, 2000 ppm, and 5000 ppm. Fig. 6(b) plots the θ_{1f} signal amplitude as a function of methane concentration, ranging

from 100 to 6000 ppm. A linear fitting to the experimental data demonstrates a good linear response with an R-squared value of 0.999.

The θ_{1f} signal of pure N_2 was continuously measured to perform an Allan-Werle deviation analysis for the long-term stability and the ultimate detection limit assessment. The measurement lasted about 4.5 hours with the results shown in Fig. 7. The Allan-Werle deviation analysis shows a minimum detection limit (MDL) of 5 ppm at a 5-second integration time, corresponding to a normalized noise equivalent absorption coefficient (NNEA) of 3×10^{-8} W·cm^{-1}·Hz$^{-1/2}$. The $1/\sqrt{t}$ correlation until 420 seconds illustrates the sensor's high stability, allowing for averaging to improve the MDL down to 0.57 ppm. The MDL, together with the maximum methane concentration, i.e., 6000 ppm, in the experiments determines a dynamic range of 5 orders of magnitude, which is comparable with most reported QEPAS or LITES sensors[22,42].

5. Conclusions and perspectives

In this article, we have presented a quartz-enhanced trace gas sensor, in which a single QTF merges the techniques of QEPAS and LITES together for enhancing its piezoelectric effect. Different from the common intensity demodulation, an alternative strategy of harmonic phase demodulation manifest itself with unique characteristics of high immunity to both laser power and demodulation phase. By demonstrating the measurement of methane in the near infrared as an example, a θ_{1f} sensor was developed with a minimum detection limit of 0.57 ppm and a
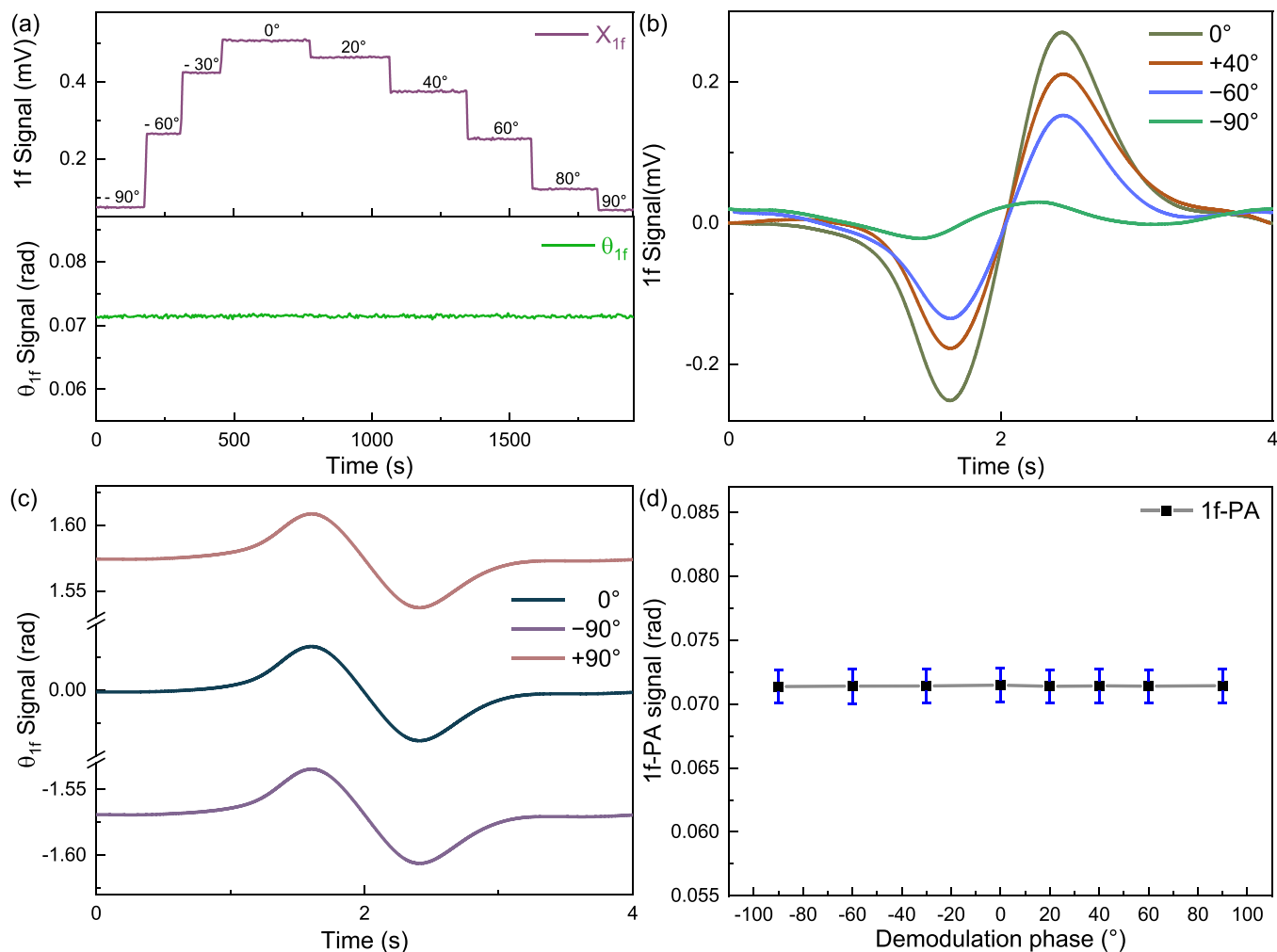

Fig. 5. (a) The influence of the demodulation phase on the 1f signal and the θ_{1f} signal. (b) Baseline-subtracted original 1f spectra and (c) θ_{1f} spectra under different demodulation phases. (d) θ_{1f} value under different demodulation phases, error bars are calculated from 20 measurements and scaled up by tenfold for clarity.
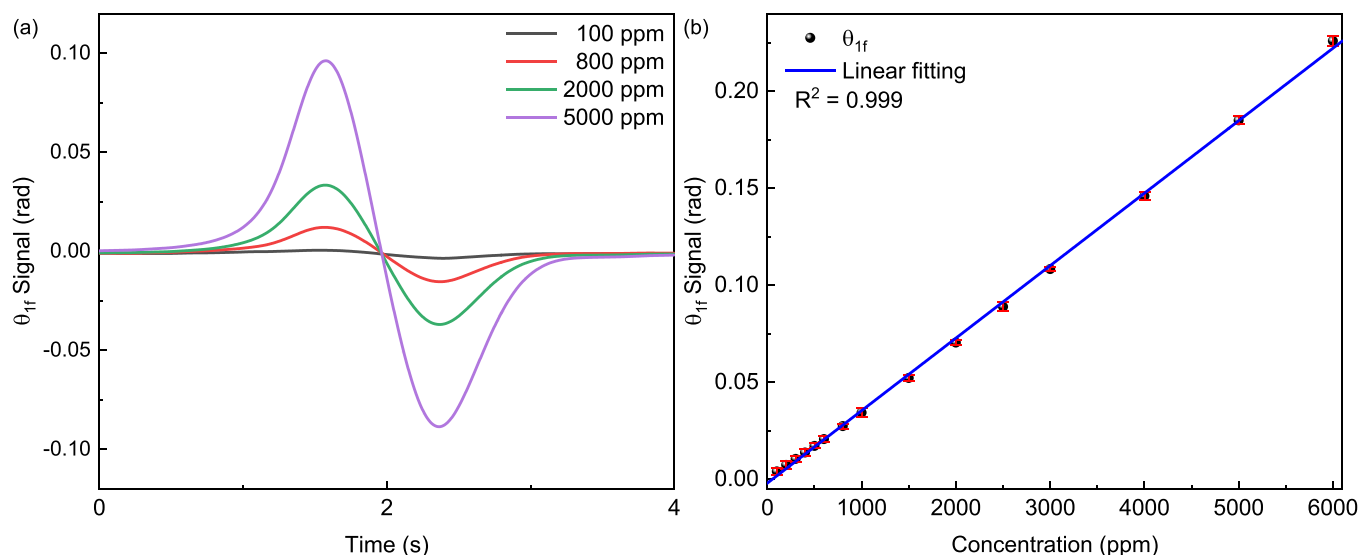
Fig. 6. (a) Baseline-subtracted θ_{1f} spectra under four representative CH_4 concentrations of 100 ppm, 800 ppm, 2000 ppm, and 5000 ppm. (b) The θ_{1f} signal amplitude as a function of methane concentration. Error bars are calculated from 20 measurements and scaled up by tenfold for clarity.
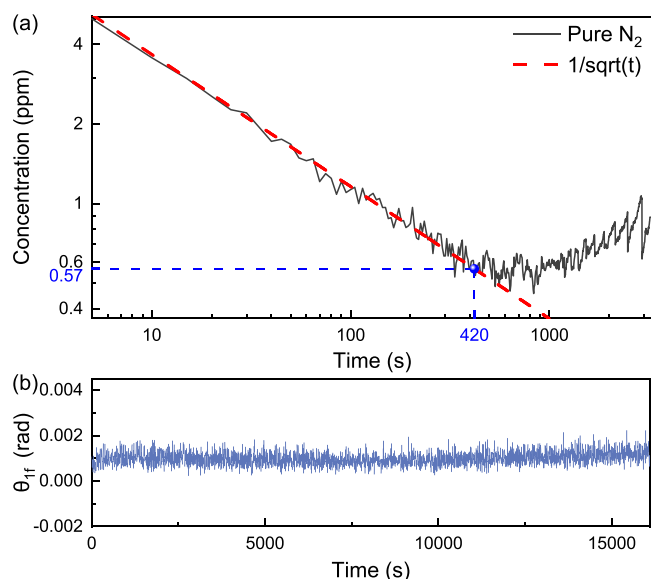

Fig. 7. (a) Allan-Werle deviation analysis of our θ_{1f}-based methane sensor as a function of integration time. The measurement was carried out with the gas cell filled with pure N_2. (b) Raw data used for Allan-Werle deviation calculation.

wide dynamic range of 5 decades. The harmonic phase demodulation achieved stable θ_{1f} measurement in the case of fluctuant laser power (2.4 mW to 9.4 mW) and demodulation phase ($-90°$ to $90°$).

In addition, the experimental investigation on the relationship between θ_{1f} SNR and laser power reveals the possibility of further sensitivity enhancement by simply employing a higher laser power. The relative flat θ_{1f} response to the modulation frequency offers much more tolerance to the resonant frequency shift of a QTF, which has always been a common but negative factor limiting its widespread application outside the laboratory. Immunity to resonant frequency shift can also be expected if the mismatch between photoacoustic and thermoelastic responses could be compensated by finely adjusting the position of the acoustic wave and light-induced thermoelastic expansion. Although our θ_{1f} gas sensor is demonstrated in the near infrared, it is possible to

extend this technique to other optical range of interest thanks to the outstanding advantage of wavelength independence for QEPAS [45] and continuously improved responsivity of custom QTFs over a wide optical range for LITES [31,51]. All the aforementioned benefits of this harmonic-phase method would make it poised to create a robust and powerful QTF-based tool for promising trace gas sensing, in particular when stable laser power, demodulation phase, even resonant frequency cannot be always maintained in field deployment.

CRediT authorship contribution statement

Weibiao Wang: Project administration, Investigation. **Qiang Wang:** Writing – review & editing, Supervision, Methodology, Funding acquisition, Conceptualization. **Hui Zhang:** Visualization, Software, Methodology. **Yu Liu:** Resources, Investigation, Funding acquisition, Formal analysis. **Mengpeng Hu:** Writing – original draft, Visualization, Validation, Investigation, Data curation, Conceptualization. **Dongqing Zhang:** Visualization, Methodology, Investigation, Formal analysis, Data curation.

Declaration of Competing Interest

The authors declare that they have no known competing financial interests or personal relationships that could have appeared to influence the work reported in this paper.

Data Availability

Data will be made available on request.

Acknowledgements

Appendix A. Detailed expression of X and Y components of the first harmonic photoacoustic and thermoelastic signals

The detailed expressions for X^{PA}_{1f}, X^{TE}_{1f}, Y^{PA}_{1f}, Y^{TE}_{1f} can be expressed as,

$$X^{PA}_{1f} = l_1(i_1 H_0 \cos(\varphi_3 - \varphi_1) + H_1 \cos(\varphi_3) + \frac{1}{2}i_1 H_2 \cos(\varphi_3 + \varphi_1)) \tag{A1}$$

$$X^{TE}_{1f} = (1 - l_2 H_0)i_1 \cos(\varphi_3 - \varphi_1 - \varphi_2) - l_2 H_1 \cos(\varphi_3 - \varphi_2) - \frac{1}{2}l_2 i_1 H_2 \cos(\varphi_3 + \varphi_1 - \varphi_2) \tag{A2}$$

$$Y^{PA}_{1f} = l_1(i_1 H_0 \sin(\varphi_3 - \varphi_1) + H_1 \sin(\varphi_3) + \frac{1}{2}i_1 H_2 \sin(\varphi_3 + \varphi_1)) \tag{A3}$$

$$Y^{TE}_{1f} = (1 - l_2 H_0)i_1 \sin(\varphi_3 - \varphi_1 - \varphi_2) - l_2 H_1 \sin(\varphi_3 - \varphi_2) - \frac{1}{2}l_2 i_1 H_2 \sin(\varphi_3 + \varphi_1 - \varphi_2) \tag{A4}$$

While the detailed expression for X^{PA0}_{1f}, X^{TE0}_{1f}, Y^{PA0}_{1f}, Y^{TE0}_{1f} when φ_3 equals to zero can be expressed as,

$$X^{PA0}_{1f} = l_1(i_1 H_0 \cos(\varphi_1) + H_1 + \frac{1}{2}i_1 H_2 \cos(\varphi_1)) \tag{A5}$$

$$X^{TE0}_{1f} = (1 - l_2 H_0)i_1 \cos(\varphi_1 + \varphi_2) - l_2 H_1 \cos(\varphi_2) - \frac{1}{2}l_2 i_1 H_2 \cos(\varphi_1 - \varphi_2) \tag{A6}$$

$$Y^{PA0}_{1f} = l_1(-i_1 H_0 \sin(\varphi_1) + \frac{1}{2}i_1 H_2 \sin(\varphi_1)) \tag{A7}$$

$$Y^{TE0}_{1f} = -(1 - l_2 H_0)i_1 \sin(\varphi_1 + \varphi_2) + l_2 H_1 \sin(\varphi_2) - \frac{1}{2}i_1 l_2 H_2 \sin(\varphi_1 - \varphi_2) \tag{A8}$$

Appendix B. θ_{1f} baselines at varying laser power and demodulation phase
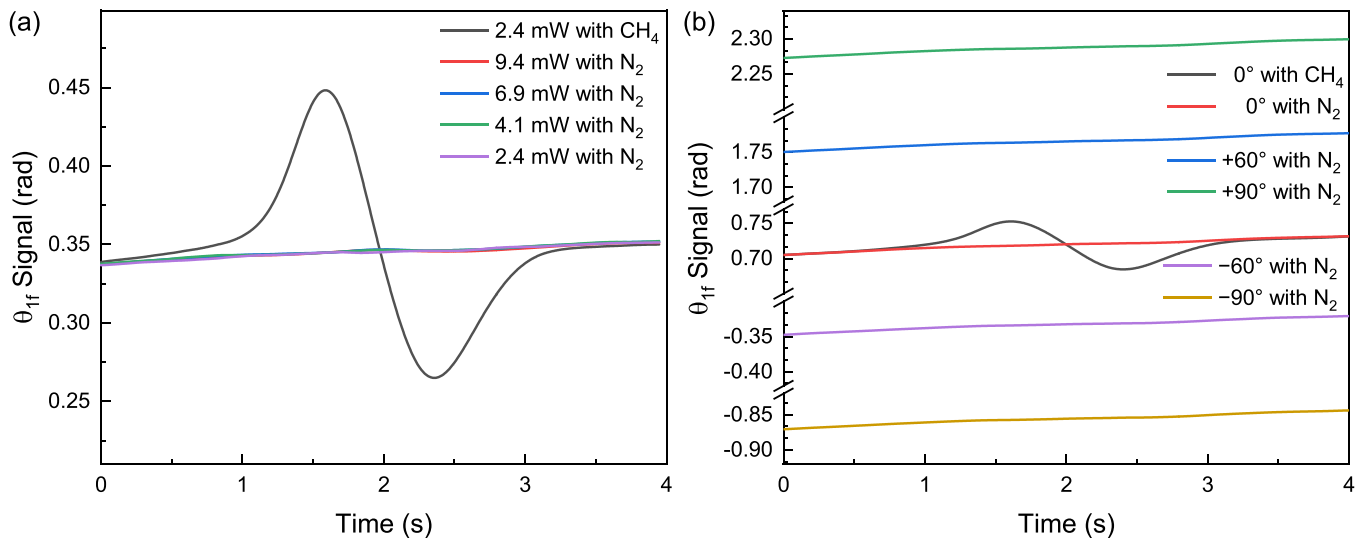

Fig. A1. Baselines of θ_{1f} signal versus **(a)** laser power and **(b)** demodulation phase.

When performing θ_{1f} spectroscopy measurement, there exist baselines for both the cases of CH$_4$ absorption and zero-absorption N$_2$. The baselines may be caused by the phase difference φ_1 between the amplitude modulation (AM) and frequency modulation (FM) of the DFB laser, which could slightly vary under different conditions of modulation current applied on a diode laser [52,53]. Fortunately, this baseline is independent from both the laser power and the demodulation phase. As shown in Fig. A1(a), the baselines with and without absorption remain rather stable under different laser power from 2.4 mW to 9.4 mW. By manually adjusting the demodulation phase φ_3, the baseline (Fig. A1(b)) merely shifts by a vertical offset accordingly without changing the slope. These results hold promise for easy baseline subtraction after only a single baseline measurement before performing gas sensing for a specific θ_{1f} spectroscopic sensor.

References

[1] K. Chen, B. Zhang, S. Liu, Q. Yu, Parts-per-billion-level detection of hydrogen sulfide based on near-infrared all-optical photoacoustic spectroscopy, Sens. Actuators B Chem. 283 (2019) 1–5, https://doi.org/10.1016/j.snb.2018.11.163.

[2] J. Shemshad, S.M. Aminossadati, M.S. Kizil, A review of developments in near infrared methane detection based on tunable diode laser, Sens. Actuators B Chem. 171 (2012) 77–92, https://doi.org/10.1016/j.snb.2012.06.018.

[3] M. Giglio, A. Zifarelli, G. Menduni, R.D. Palo, M.D. Gioia, A. Sampaolo, P. Patimisco, V. Spagnolo, Recent advances in quartz-enhanced photoacoustic spectroscopy for environmental monitoring applications, in: Opt. Sens. Sens.

Congr. 2022 AIS LACSEA Sens. ES 2022 Pap. LW4D1, Optica Publishing Group, 2022, p. LW4D.1, https://doi.org/10.1364/LACSEA.2022.LW4D.1.

[4] G. Wysocki, Y. Bakhirkin, S. So, F.K. Tittel, C.J. Hill, R.Q. Yang, M.P. Fraser, Dual interband cascade laser based trace-gas sensor for environmental monitoring, Appl. Opt. 46 (2007) 8202–8210, https://doi.org/10.1364/AO.46.008202.

[5] X. Yin, H. Wu, L. Dong, B. Li, W. Ma, L. Zhang, W. Yin, L. Xiao, S. Jia, F.K. Tittel, ppb-level SO2 photoacoustic sensors with a suppressed absorption–desorption effect by using a 7.41 μm external-cavity quantum cascade laser, ACS Sens 5 (2020) 549–556, https://doi.org/10.1021/acssensors.9b02448.

[6] M. Righettoni, A. Amann, S.E. Pratsinis, Breath analysis by nanostructured metal oxides as chemo-resistive gas sensors, Mater. Today 18 (2015) 163–171, https://doi.org/10.1016/j.mattod.2014.08.017.

[7] H. Tai, S. Wang, Z. Duan, Y. Jiang, Evolution of breath analysis based on humidity and gas sensors: Potential and challenges, Sens. Actuators B Chem. 318 (2020) 128104, https://doi.org/10.1016/j.snb.2020.128104.

[8] A.A. Kosterev, Y.A. Bakhirkin, R.F. Curl, F.K. Tittel, Quartz-enhanced photoacoustic spectroscopy, Opt. Lett. 27 (2002) 1902–1904, https://doi.org/10.1364/OL.27.001902.

[9] Y. Ma, Y. He, Y. Tong, X. Yu, F.K. Tittel, Quartz-tuning-fork enhanced photothermal spectroscopy for ultra-high sensitive trace gas detection, Opt. Express 26 (2018) 32103–32110, https://doi.org/10.1364/OE.26.032103.

[10] H. Yi, O. Laurent, S. Schilt, M. Ramonet, X. Gao, L. Dong, W. Chen, Simultaneous monitoring of atmospheric CH4, N2O, and H2O using a single gas sensor based on Mid-IR quartz-enhanced photoacoustic spectroscopy, Anal. Chem. (2022), https://doi.org/10.1021/acs.analchem.2c03785.

[11] Z. Wang, Q. Wang, H. Zhang, S. Borri, I. Galli, A. Sampaolo, P. Patimisco, V. L. Spagnolo, P. De Natale, W. Ren, Doubly resonant sub-ppt photoacoustic gas detection with eight decades dynamic range, Photoacoustics 27 (2022) 100387, https://doi.org/10.1016/j.pacs.2022.100387.

[12] G. Menduni, High-concentration methane and ethane QEPAS detection employing partial least squares regression to filter out energy relaxation dependence on gas matrix composition, (2022) 11. https://doi.org/10.1016/j.pacs.2022.100349.

[13] Y. Ma, Y. Hu, S. Qiao, Z. Lang, X. Liu, Y. He, V. Spagnolo, Quartz tuning forks resonance frequency matching for laser spectroscopy sensing, Photoacoustics 25 (2022) 100329, https://doi.org/10.1016/j.pacs.2022.100329.

[14] H. Wu, L. Dong, H. Zheng, Y. Yu, W. Ma, L. Zhang, W. Yin, L. Xiao, S. Jia, F. K. Tittel, Beat frequency quartz-enhanced photoacoustic spectroscopy for fast and calibration-free continuous trace-gas monitoring, Nat. Commun. 8 (2017) 15331, https://doi.org/10.1038/ncomms15331.

[15] S. Qiao, P. Ma, V. Tsepelin, G. Han, J. Liang, W. Ren, H. Zheng, Y. Ma, Super tiny quartz-tuning-fork-based light-induced thermoelastic spectroscopy sensing, Opt. Lett. 48 (2023) 419–422, https://doi.org/10.1364/OL.482351.

[16] Y. Ma, T. Liang, S. Qiao, X. Liu, Z. Lang, Highly sensitive and fast hydrogen detection based on light-induced thermoelastic spectroscopy, Ultra Sci. 3 (2023) 0024, https://doi.org/10.34133/ultrafastscience.0024.

[17] Y. Hu, S. Qiao, Y. He, Z. Lang, Y. Ma, Quartz-enhanced photoacoustic-photothermal spectroscopy for trace gas sensing, Opt. Express 29 (2021) 5121–5127, https://doi.org/10.1364/OE.418256.

[18] H. Wu, L. Dong, H. Zheng, X. Liu, X. Yin, W. Ma, L. Zhang, W. Yin, S. Jia, F.K. Tittel, Enhanced near-infrared QEPAS sensor for sub-ppm level H2S detection by means of a fiber amplified 1582 nm DFB laser, Sens. Actuators B Chem. 221 (2015) 666–672, https://doi.org/10.1016/j.snb.2015.06.049.

[19] H. Lv, H. Zheng, Y. Liu, Z. Yang, Q. Wu, H. Lin, B.A.Z. Montano, W. Zhu, J. Yu, R. Kan, Z. Chen, F.K. Tittel, Radial-cavity quartz-enhanced photoacoustic spectroscopy, Opt. Lett. 46 (2021) 3917–3920, https://doi.org/10.1364/OL.432308.

[20] H. Wu, X. Yin, L. Dong, K. Pei, A. Sampaolo, P. Patimisco, H. Zheng, W. Ma, L. Zhang, W. Yin, Simultaneous dual-gas QEPAS detection based on a fundamental and overtone combined vibration of quartz tuning fork, Appl. Phys. Lett. 110 (2017), https://doi.org/10.1063/1.4979085.

[21] K. Liu, X. Guo, H. Yi, W. Chen, W. Zhang, X. Gao, Off-beam quartz-enhanced photoacoustic spectroscopy, Opt. Lett. 34 (2009) 1594, https://doi.org/10.1364/OL.34.001594.

[22] K. Liu, H. Yi, A.A. Kosterev, W. Chen, L. Dong, L. Wang, T. Tan, W. Zhang, F. K. Tittel, X. Gao, Trace gas detection based on off-beam quartz enhanced photoacoustic spectroscopy: optimization and performance evaluation, Rev. Sci. Instrum. 81 (2010) 103103, https://doi.org/10.1063/1.3480553.

[23] Y. Ma, X. Yu, G. Yu, X. Li, J. Zhang, D. Chen, R. Sun, F.K. Tittel, Multi-quartz-enhanced photoacoustic spectroscopy, Appl. Phys. Lett. 107 (2015) 021106, https://doi.org/10.1063/1.4927057.

[24] S. Qiao, Y. Ma, P. Patimisco, A. Sampaolo, Y. He, Z. Lang, F.K. Tittel, V. Spagnolo, Multi-pass quartz-enhanced photoacoustic spectroscopy-based trace gas sensing, Opt. Lett. 46 (2021) 977–980, https://doi.org/10.1364/OL.418520.

[25] Y. Cao, W. Jin, L.H. Ho, Z. Liu, Evanescent-wave photoacoustic spectroscopy with optical micro/nano fibers, Opt. Lett. 37 (2012) 214–216, https://doi.org/10.1364/OL.37.000214.

[26] Z. Li, Z. Wang, Y. Qi, W. Jin, W. Ren, Improved evanescent-wave quartz-enhanced photoacoustic CO sensor using an optical fiber taper, Sens. Actuators B Chem. 248 (2017) 1023–1028, https://doi.org/10.1016/j.snb.2017.03.029.

[27] W. Feng, Y. Qu, Y. Gao, Y. Ma, Advances in fiber-based quartz enhanced photoacoustic spectroscopy for trace gas sensing, Microw. Opt. Technol. Lett. 63 (2021) 2031–2039, https://doi.org/10.1002/mop.32841.

[28] P. Patimisco, A. Sampaolo, L. Dong, M. Giglio, G. Scamarcio, F.K. Tittel, V. Spagnolo, Analysis of the electro-elastic properties of custom quartz tuning forks for optoacoustic gas sensing, Sens. Actuators B Chem. 227 (2016) 539–546, https://doi.org/10.1016/j.snb.2015.12.096.

[29] M. Duquesnoy, G. Aoust, J.-M. Melkonian, R. Lévy, M. Raybaut, A. Godard, Quartz enhanced photoacoustic spectroscopy based on a custom quartz tuning fork, Sensors 19 (2019) 1362, https://doi.org/10.3390/s19061362.

[30] H. Zhang, Z. Wang, Q. Wang, S. Borri, I. Galli, A. Sampaolo, P. Patimisco, V. L. Spagnolo, P. De Natale, W. Ren, Parts-per-billion-level detection of hydrogen sulfide based on doubly resonant photoacoustic spectroscopy with line-locking, Photoacoustics 29 (2023) 100436, https://doi.org/10.1016/j.pacs.2022.100436.

[31] T.T. Wei, A. Zifarelli, S. Dello Russo, H.P. Wu, G. Menduni, P. Patimisco, A. Sampaolo, V. Spagnolo, L. Dong, High and flat spectral responsivity of quartz tuning fork used as infrared photodetector in tunable diode laser spectroscopy, Appl. Phys. Rev. 8 (2021) 041409, https://doi.org/10.1063/5.0062415.

[32] S. Qiao, Y. He, Y. Ma, Trace gas sensing based on single-quartz-enhanced photoacoustic–photothermal dual spectroscopy, Opt. Lett. 46 (2021) 2449–2452, https://doi.org/10.1364/OL.423801.

[33] X. Yin, L. Dong, H. Wu, H. Zheng, W. Ma, L. Zhang, W. Yin, S. Jia, F.K. Tittel, Sub-ppb nitrogen dioxide detection with a large linear dynamic range by use of a differential photoacoustic cell and a 3.5 W blue multimode diode laser, Sens. Actuators B Chem. 247 (2017) 329–335, https://doi.org/10.1016/j.snb.2017.03.058.

[34] Y. Ma, Y. Tong, Y. He, X. Yu, F.K. Tittel, High-power DFB diode laser-based CO-QEPAS sensor: optimization and performance, Sensors 18 (2018) 122.

[35] Y. Ma, Y. He, Y. Tong, X. Yu, F.K. Tittel, Ppb-level detection of ammonia based on QEPAS using a power amplified laser and a low resonance frequency quartz tuning fork, Opt. Express 25 (2017) 29356–29364, https://doi.org/10.1364/OE.25.029356.

[36] R. Lewicki, G. Wysocki, A.A. Kosterev, F.K. Tittel, Carbon dioxide and ammonia detection using 2 μm diode laser based quartz-enhanced photoacoustic spectroscopy, Appl. Phys. B 87 (2007) 157–162, https://doi.org/10.1007/s00340-006-2474-9.

[37] H. Liu, X. Chen, L. Yao, Z. Xu, M. Hu, R. Kan, Simultaneous detection of gas concentration and light intensity based on dual-quartz-enhanced photoacoustic-photothermal spectroscopy, Photonics 10 (2023) 165, https://doi.org/10.3390/photonics10020165.

[38] L. Xu, J. Li, N. Liu, S. Zhou, Quartz crystal tuning fork based 2f/1f wavelength modulation spectroscopy, Spectrochim. Acta Mol. Biomol. Spectrosc. 267 (2022) 120608, https://doi.org/10.1016/j.saa.2021.120608.

[39] W.Y. Peng, C.L. Strand, R.K. Hanson, Analysis of laser absorption gas sensors employing scanned-wavelength modulation spectroscopy with 1 f-phase detection, Appl. Phys. B 126 (2020) 1–23, https://doi.org/10.1007/s00340-019-7369-7.

[40] D.C. Dumitras, D. Dutu, C. Matei, A.-M. Bratu (Magureanu), M. Petrus, C. Popa, Laser photoacoustic spectroscopy: Principles, instrumentation, and characterization, J. Optoelectron. Adv. Mater. 9 (2007) 3655–3701.

[41] X. Zhang, L. Liu, L. Zhang, X. Yin, H. Huan, L. Zhang, X. Shao, A compact portable photoacoustic spectroscopy sensor for multiple trace gas detection, J. Appl. Phys. 131 (2022) 174501, https://doi.org/10.1063/5.0088257.

[42] Y. He, Y. Ma, Y. Tong, X. Yu, F.K. Tittel, Ultra-high sensitive light-induced thermoelastic spectroscopy sensor with a high Q-factor quartz tuning fork and a multipass cell, Opt. Lett. 44 (2019) 1904–1907, https://doi.org/10.1364/OL.44.001904.

[43] Q.D. Zhang, J. Chang, Z.H. Cong, Z.L. Wang, Application of quartz tuning fork in photodetector based on photothermal effect, IEEE Photonics Technol. Lett. 31 (2019) 1592–1595, https://doi.org/10.1109/Lpt.2019.2939046.

[44] C. Yang, L. Mei, H. Deng, Z. Xu, B. Chen, R. Kan, Wavelength modulation spectroscopy by employing the first harmonic phase angle method, Opt. Express 27 (2019) 12137–12146, https://doi.org/10.1364/OE.27.012137.

[45] P. Patimisco, A. Sampaolo, L. Dong, F.K. Tittel, V. Spagnolo, Recent advances in quartz enhanced photoacoustic sensing, Appl. Phys. Rev. 5 (2018), https://doi.org/10.1063/1.5013612.

[46] S. Schilt, L. Thévenaz, Wavelength modulation photoacoustic spectroscopy: theoretical description and experimental results, Infrared Phys. Technol. 48 (2006) 154–162, https://doi.org/10.1016/j.infrared.2005.09.001.

[47] X. Li, F. Yuan, M. Hu, B. Chen, Y. He, C. Yang, L. Shi, R. Kan, Compact open-path sensor for fast measurements of CO2 and H2O using scanned-wavelength modulation spectroscopy with 1f-phase method, Sens. Basel 20 (2020) 1910, https://doi.org/10.3390/s20071910.

[48] A. Castellanos-Gomez, N. Agraït, G. Rubio-Bollinger, Force-gradient-induced mechanical dissipation of quartz tuning fork force sensors used in atomic force microscopy, Ultramicroscopy 111 (2011) 186–190, https://doi.org/10.1016/j.ultramic.2010.11.032.

[49] A. Naber, The tuning fork as sensor for dynamic force distance control in scanning near-field optical microscopy, J. Microsc. 194 (1999) 307–310, https://doi.org/10.1046/j.1365-2818.1999.00548.x.

[50] H. Zhang, W. Jin, M. Hu, H. Liang, Q. Wang, Investigation and optimization of a line-locked quartz enhanced spectrophone for rapid carbon dioxide measurement, Sensors 21 (2021) 5225, https://doi.org/10.3390/s21155225.

[51] C. Lou, X. Liu, Y. Wang, Y. Zhang, Y. Li, J. Yao, C. Chang, Y. Ma, X. Liu, Ultra-broadband optical detection from the visible to the terahertz range using a miniature quartz tuning fork, Opt. Lett. 47 (2022) 1875–1878, https://doi.org/10.1364/OL.452984.

[52] J. Li, Z. Du, Y. An, Frequency modulation characteristics for interband cascade lasers emitting at 3 μm, Appl. Phys. B 121 (2015) 7–17, https://doi.org/10.1007/s00340-015-6195-9.

[53] W. Lenth, High frequency heterodyne spectroscopy with current-modulated diode lasers, IEEE J. Quantum Electron. 20 (1984) 1045–1050, https://doi.org/10.1109/JQE.1984.1072505.

Mengpeng Hu received his B.S. degree from Dalian University of Technology in 2019. He is currently a PhD student at Changchun Institute of Optics, Fine Mechanics and Physics, Chinese Academy of Sciences. His research interests are photothermal spectroscopy and laser frequency comb.

Dongqing Zhang received her B.S. degree from University of Jinan in 2022. She is currently a master student at Changchun Institute of Optics, Fine Mechanics and Physics, Chinese Academy of Sciences. Her research interest is cavity enhanced absorption spectroscopy.

Hui Zhang received his BEng degree from Ocean University of China in 2019. He is currently a PhD student at Changchun Institute of Optics, Fine Mechanics and Physics, Chinese Academy of Sciences. His research project is on gas sensing and cavity enhanced photoacoustic spectroscopy.

Yu Liu is currently an associate professor at Changchun Institute of Optics, Fine Mechanics and Physics, Chinese Academy of Sciences. He received his B.S. degree in Optical Information Science and Technology in 2006 and Ph.D. degree in Physical Chemistry 2011 from Jilin University. His recent research interests are laser spectroscopy, Raman spectroscopy, and the application of spectroscopy in agriculture.

Weibiao Wang is currently a professor in the State Key Laboratory of Applied Optics at Changchun Institute of Optics, Fine Mechanics and Physics, Chinese Academy of Sciences. He received his Ph.D. degree in Changchun Institute of Optics, Fine Mechanics and Physics, Chinese Academy of Sciences in 1999. His research activities included optoelectronic materials and devices, photodetectors, light emitting diode (LED) array chip integration and applications, photonic crystals, and micronano photonics.

Qiang Wang is currently a professor in the State Key Laboratory of Applied Optics at Changchun Institute of Optics, Fine Mechanics and Physics, Chinese Academy of Sciences. He received his B.S. degree in Electronic Science and Technology in 2011 and Ph.D. degree in Optical Engineering in 2016 from Shandong University. After his graduate study, he worked as a postdoctoral fellow at the Chinese University of Hong Kong and Max Planck Institute of Quantum Optics successively. His recent research interests are laser spectroscopy, optical sensing, and engineering application of trace gas analysis in the atmosphere, deep sea, and public health.